Simulations and Experiments on Low-Pressure Permeation of Fabrics: Part II—The Variable Gap Model and Prediction of Permeability

M. T. SENOGUZ, F. D. DUNGAN, A. M. SASTRY[1] AND J. T. KLAMO
Department of Mechanical Engineering
2140 G.G. Brown Building
2350 Hayward Street
The University of Michigan
Ann Arbor, MI 48109-2125

ABSTRACT: Use of the creeping flow assumption provides a computationally efficient and accurate means of predicting flow fronts in reinforcement media in many technologically important polymer processes. In the case of fabrics, this creeping flow is shown to proceed primarily through the gaps in fabrics, with capillarity playing little if any role for commonly used materials. This finding has important implications for selection of strategy in modeling manufacturing processes of such materials. Namely, in the presence of fabric deformation which induces local shear, changes in the gap architecture greatly affect the flow patterns, and are not well predicted by tensor transformation of Darcy-type permeabilities. A simple, classic flow model is adapted to the case of fabrics penetrated by low-pressure viscous liquids after careful analysis of fabric architecture. An applicability range of this creeping flow model, the variable gap model, is developed. The present paper gives the model assumptions, and confirmation of its agreement with more sophisticated calculations. A demonstration of the approach for an unbalanced fabric (Knytex 24 5×4 unbalanced plain-woven glass fabric) shows excellent prediction of the bounds on flow behavior, and supports our earlier experimental findings on flow front orientation. This approach also shows clear superiority to semi-empirical, geometry-based models, since no fitting parameters at all are used in the modeling: only the constituent materials' geometry and properties are needed. This methodology is better able to predict trends in flow fronts, both qualitatively and quantitatively, than semi-empirical fitting. Extension of this work to realistic production processes is planned.

[1]Author to whom correspondence should be addressed. E-mail: amsastry@umich.edu

0021-9983/01/14 1285–38 $10.00/0 DOI: 10.1106/HWL5-599F-8NA8-XAN0

Journal Online at http://techpub.metapress.com

INTRODUCTION

LOW-PRESSURE PENETRATION OF fabrics by viscous fluid is a key phenomenon in many technologically important composite processes. The majority of parts involved presents some degree of curvature. Thus, development of a robust description of fabrics is crucial for fabrics undergoing deformation (primarily shear). In the first part of this work (Dungan et al., 2001), a 3D model for an unbalanced plain-woven fabric was developed. This was motivated by the failure of simple geometry models or empirical models to predict permeability of such fabrics in shear. In this part of the work, we use the newly developed fabric model to predict permeability of fabric in both sheared and unsheared configurations, using an approximation for flow channel shape in the fabric. This model, unlike previous approaches used in predicting fabric permeability in either sheared or unsheared configurations, employs no fitting parameters.

Flow through reinforcements and between layers is hypothesized here to present a complex flow path which requires more detailed modeling than the common empirical or geometric modifications to Darcy's law, including the Carman-Kozeny equation, which typically involve calculation of permeabilities of the woven fabrics using fiber radius, overall volume fraction, and some empirically-determined constants. In the regions where the volume fraction is high, the increased fiber surface area with respect to the gap area creates a high viscous shear force, which reduces apparent permeability. Conversely, high ratios of surface area to gap area enhance capillary flow. This additional driving force, acting on the surface of the fluid, increases the permeability of the media, motivating our study of the effect of capillary pressure as a momentum source. Use of a linear flow theory allows development of an equivalent expression for these permeabilities.

Experimentation on three scales was performed in the present study to assess the relative importance of these phenomena: (1) single fiber contact angle measurements; (2) tow-level capillary pressure experiments; and (3) radial fabric-level permeability experiments. Each of these gave insight into the flow dynamics at the microscale, and motivated some significant aspect of the numerical study. The single fiber experiments allowed calculation of the static contact angle, and thus a calculation of capillary pressure in a tow. The tow impregnation experiments allowed determination of intratow permeability, using the capillary pressure determined via contact angles. The radial permeability experiments with sheared and unsheared fabrics gave us insight into the effects of changing geometry on the overall fabric permeability.

Simulations were performed on two scales. First, a full Navier-Stokes simulation for flow in a gap/tow region was performed. Second, a simplified flow calculation based directly on information from the fabric model was developed to calculate permeabilities by considering only flow in the gap regions. Finally, we

compare our linear model based on fabric architecture to experimental permeability data, and discuss the range of applicability and possible improvements to the model.

ANALYSIS OF KEY EFFECTS IN RTM PROCESSES

Overview of Previous Work

Some simplification in the modeling of resin flow through the interstices and between layers of fiber beds is necessitated by the present impracticality of numerically solving the full Navier-Stokes equations in a stochastically- or near-regularly-arranged array of inclusions in the path of the flow front (e.g., Sastry, 2000). Percolation (i.e., low Reynolds number, Newtonian flows in macroscopically homogeneous domains) was described originally by Darcy (1856), who developed the constitutive description by observing water flow through beds of sand. Application of Darcy's model to composite processes, from laminates to molded materials, is widespread. The percolation flow is generally applied to thermosetting resins in autoclave (laminate) or liquid molding processes. The familiar Darcy model may be written

$$\bar{v} = \frac{-K}{\mu} \nabla P \tag{1}$$

where $\bar{v}$ is the average fluid velocity, μ is the fluid viscosity, K is the permeability of the porous medium, and ∇P is the pressure gradient and can be written in tensorial form for anisotropic preforms, where up to 3 scalar permeabilities are required in the plane case. Such implementations thus require determination of the permeability or components of a permeability tensor, via experimental or theoretical means. In application to actual processing, various factors are commonly used to account for flow "tortuosity," or circuitousness of the path that must be traversed to penetrate the material, the shape of the particles, material anisotropy, and the average volume fraction. Several modifications to Equation (1) have thus been proposed in the polymer processing arena and in other areas of fluid-structure interaction; for example, Kozeny (1927) treated a permeated porous medium as a bundle of capillary tubes and obtained a relationship to adapt Darcy's law to include capillarity effects with an empirical relation; Blake (1922) derived a similar expression. Carman (1937) modified Kozeny's work by defining S, the specific surface with respect to a unit volume of solid, instead of a unit volume of porous medium. The "Kozeny-Carman relationship" arose through these sequential contributions. Carman (1937) experimentally determined a range of "Kozeny constants" for a variety of packing schemes and geometries of reinforcements. This constant is determined empirically from

$$K = \frac{r_f^2}{4c} \frac{(1 - V_f)^3}{V_f^2} \tag{2}$$

where V_f is the fiber volume fraction, c is a constant based on the geometric form of the fibrous bed, and r_f is the fiber diameter.

Such relations have commonly been used to model polymeric flow in composite materials in the last 20 years (see, for example, the review by Coulter and Guceri, 1988). Williams et al. (1974) considered the flow of several fluids through aligned reinforcements, both dry and pre-saturated with liquid. They obtained higher permeabilities for saturated than for unsaturated reinforcement, as did Martin and Son (1986). Many authors since the late 1980s have specifically studied the permeability of fibrous preforms for liquid molding, including Parnas et al. (1997), Adams and Rebenfeld (1991a,b), Gauvin et al. (1996), Chan et al. (1993), Gebart (1992), Rudd et al. (1996), Skartsis et al. (1992a,b), Young and Wu (1995) and Mogavero and Advani (1997). More recent work has focused on complex geometries. In 1996, Rudd et al. established a "permeability map" for complex geometries. Smith et al. (1997) related permeabilities of sheared fabrics to ply angle. Lai and Young (1997) related similar experimental data to a geometry-based flow model.

Other closed-form modifications to Darcy's law have been developed to relate volume fraction and geometric or empirical constants such as the maximum packing fraction to the permeability of a periodic medium comprised of parallel cylinders. Gebart (1992) derived an equivalent permeability based on the assumption of hexagonally-arranged fibers. Cai and Berdichevsky (1993) extended a classic self-consistent approach, wherein a heterogeneous element was assumed to be embedded in an equivalent homogeneous medium. The homogeneous medium was constructed such that the total flow and dissipation energy remained the same. Use of a no-slip boundary condition at the fiber surface and zero velocity gradient in the radial direction at the domain boundaries resulted in an equivalent permeability value. The improved self-consistent method (Berdichevsky and Cai, 1993) took into account an additional parameter V_A, the maximum packing capacity of fibers, to increase the accuracy of the model. Bruschke and Advani (1993) developed a closed-form solution for permeability by matching the lubrication solution for low porosities and an analytical cell model solution for high porosities. They found agreement between their hybrid, arrangement-specific closed-form solution and a numerical solution of the Navier-Stokes equations for flow around both hexagonal and square arrangements of cylinders (using a simulation package, POLYFLOW). Van der Westhuizen and Du Plessis (1996) used phase-averaged Navier-Stokes equations to calculate the permeability of representative unit cells, and reported agreement with experimental in-plane permeabilities. Their model did not assume any particular arrangement of fibers for longitudinal permeability,

but used the maximum packing capacity for different arrangements of fibers to create an effective volume fraction for transverse permeability. Wang (1996) developed a similar relation for an array of rectangularly-packed fibers. Table 1 gives a comparison of some of these semi-empirical techniques.

Computational fluid dynamics software can be used to solve the full Navier-Stokes equations to determine flow progression, although practically this can be done only for small domains. Several workers have developed intermediate special-purpose codes to model fluid flow in fabrics that account for effects such as capillarity, race tracking, saturation, etc. For example, Advani and co-workers developed "LIMS," (e.g., Pillai and Advani, 1998; Bruschke and Advani, 1990) which is able to simulate edge effects by implementation of a mass sink to the continuity equation to account for saturation. Pillai and Advani (1998) implemented the continuity equation as

Table 1. Fabric permeability relationships developed by various workers.

	Axial Permeability	Transverse Permeability
Gebart (1992)	$K_x = \frac{8r_f^2}{53}\frac{(1-V_f)^3}{V_f^2}$	$K_z = \frac{16}{9\pi\sqrt{6}}\left(\sqrt{\frac{V_A}{V_f}}-1\right)^{2.5} * r_f^2$
Cai and Berdichevsky (1993)	$K_x = \frac{r_f^2}{8V_f} * \left[\ln\frac{1}{V_f^2} - (3-V_f)(1-V_f)\right]$	$K_z = \frac{r_f^2}{8V_f}\left[\ln\frac{1}{V_f} - \frac{1-V_f^2}{1+V_f^2}\right]$
Berdichevsky and Cai (1993)	$K_x = 0.111\frac{r_f^2}{V_f} * \ln\left(\frac{1}{V_f}\right)\exp[-1.54V_f - 2.82V_f^2]$	$K_z = 0.229r_f^2\left(\frac{1.814}{V_A}-1\right) * \left[\frac{1-\sqrt{V_f/V_A}}{V_f/V_A}\right]^{2.5}$
Bruschke and Advani (1993)	Not applicable	$K_z = \frac{r_f^2}{3\sqrt{3}}\frac{(1-l^2)^2}{l^3} * \left(3l\frac{\arctan(\sqrt{(1+l)/(1-l)})}{\sqrt{1-l^2}} + \frac{l^2}{2} + 1\right)^{-1}$ $l^2 = \frac{2\sqrt{3}}{\pi}(1-\varepsilon)$
Van der Westhuizen and Du Plessis (1996)	$K_x = r_f^2 * \frac{(5.299 - 2.157\varepsilon)\varepsilon^2}{48(1-\varepsilon)^2}$	$K_z = r_f^2 * \frac{\pi(1-V_f^*)\cdot(1-\sqrt{V_f^*})^2}{24(V_f^*)^{1.5}}$ $V_f^* = 2.22(V_f)^2 - 122V_f + 0.56$

$$\nabla \cdot \left(\frac{K}{\mu} \cdot \nabla P \right) = \left(\frac{\varepsilon}{\left(\frac{r_{2A}}{r_{1A}} \right)^2 - 1} \right) \frac{2 r_{fA} (-\dot{r}_{fA})}{r_{1A}^2} \tag{3}$$

where r_{fA} is the micro-front radius in the sink and r_{1A} and r_{2A} are the tow and cell radii, respectively. The right hand side of the equation, denoted S_A, is the strength of a type A sink, calculated as

$$\dot{r}_{fA} = - \frac{K_{it} \cdot P}{\varepsilon \mu r_{fA} \ln \left(\frac{r_{1A}}{r_{fA}} \right)} \tag{4}$$

where K_{it} is the tow permeability. "Front Tracking" is capable of simulating the formation of voids (Song et al., 1997) and "SIMTEC" (Lin et al., 1998) accounts for capillary action. "SUPERTM" is another interactive filling simulation (Ismail and Springer, 1997). Chang and Hourng (1998) developed a two-dimensional model for tow impregnation, taking into account micro/macroscopic flow and void formation. Ambrosi and Preziosi (1998) developed a model for flow dynamics in an elastically deforming environment.

Flow in tows versus gaps or voids has been specifically studied by a number of workers. Shih and Lee (1998), for example, used six different types of glass fiber reinforcements to determine the effect of fiber architecture on apparent permeability. The reinforcements included 4-harness woven, plain weave, random fiber and stitched fiber mats. They argued that the gap size between the tows and the connectivity of the gaps control permeability. Kolodziej et al. (1998) proposed a theoretical model which accounted specifically for gaps as caverns or fissures inside the bundle of fibers. Both diameter of fibers and also diameter of gaps inside the fiber bundles were incorporated in the model. They reported that tow heterogeneity can decrease or increase tow permeability, depending on the critical dimensionless radius of these gaps. Heterogeneity was identified as the probable cause of deviation of permeabilities from permeability models, which assume uniformity inside the fiber bundles.

Capillarity has been advanced by a number of workers as an explanation for enhanced flow in fabrics. Analytical and numerical estimates of its relative importance have been made by a number of workers. Lekakou and Bader (1998), for example, modeled macro- and micro-flow, including capillary pressure. They performed numerical parametric studies to correlate the effects of inter-tow and intra-tow volume fractions, different pressures, and fiber diameters on apparent permeabilities. Hourng and Chang (1998) investigated edge flow and the effect of capillary pressure on edge flow. They suggested that for edges larger than the criti-

cal value of $2K^{0.5}$, where K is the permeability, the edge effect cannot be neglected. Using numerical simulations, Chang et al. (1998) stated that the capillary effect is limited to capillary numbers less than $O(10^{-2})$. The capillary number, given by

$$Ca = \frac{\mu - v}{\sigma} \tag{5}$$

is the ratio of viscous forces to surface forces. A small capillary number represents strong capillary action. Hourng and Chang (1998) proposed that capillarity be neglected for conventional RTM processes which usually have higher injection pressures than 10 kPa. Ahn et al. (1991) experimentally observed that pressure dependence in capillarity begins around $Ca \sim O(10^{-6})$. In his numerical study, Young (1996) reported that below a critical capillary number, the fluid in the tows moves faster than the fluid between the tows because of the additional capillary pressure. Conversely, above the critical capillary number, the flow between the tows dominates. The critical number was found to be 1×10^{-4} though he cautioned that this number might change for different preform types.

Determination of capillary pressure is generally made using the solid/liquid (droplet) contact angle. Dynamic effects cause the contact angle to deviate from the static capillary pressure. It is generally difficult to measure the dynamic angle, but Skartsis et al. (1992c) proposed that for capillary number up to $O(10^{-4})$, the static contact angle provided an excellent approximation to the dynamic contact angle. Thus, for Re < 3000, such as creeping flow in porous medium, he suggested use of static contact angle rather than dynamic contact angle. These relationships and assumptions have been tested experimentally. For example, Ahn et al. (1991) measured permeability and capillary pressures simultaneously by controlling both positive pressure at the inlet and pressure against the flow in the mold. By finding the negative piston pressure preventing flow front penetration in the fabric, the capillary pressure for that fabric was found. They reported capillary pressures as high as 37 kPa for T-300 carbon fibers, concluding that although capillary pressure is negligible for an injection process, it may be important for low pressure processes such as prepregging. They also observed that the Carman-Kozeny estimation of permeability deviated from the experimental results for high porosity fabrics, while the Young-Laplace equation [see Equation (6) below] gave consistent results with experiments for capillary pressure.

Previous studies on RTM with fabrics have thus emphasized various manufacturing factors, but most have implemented flow models in which pressure gradient and velocity are related linearly, with corrections for surface and geometry effects. We now examine the underlying contribution of surface effects, specifically

capillarity, by analytical means. First, we develop equivalence relationships for various creeping flows, in order to compare the gap and intra-tow permeabilities for a fabric. We then compare these calculations with experiments in the fabric system considered in this two-part work, i.e., Knytex 24 5×4 unbalanced plain-woven glass fabric.

Comparison of Creeping Flows and Model Development

The proportionality of velocity and pressure gradient is central to modeling classic creeping flows wherein the scaling parameter, "permeability," may be derived as in Table 2. Schematics of each case are given as Figure 1. "Plane Poiseuille flow" describes steady-state flow between two infinitely long parallel plates separated by a distance $2b$ (e.g., Kundu, 1990). Circular Poiseuille flow refers to steady flow in a tube of diameter d. Flow in a channel of linearly varying thickness describes flow in a channel with inlet half-thickness a_1, outlet half-thickness a_2, and channel length L (e.g., Batchelor, 1967). We hereafter refer to the model just described [Figure 1(d) and last line of Table 2] as the VGM, or Variable Gap Model. In the sections that follow, we describe a technique for reducing information from a 3D fabric model (developed in Part I of this work, Dungan et al., 2001) to 2D sections, to a 1D model, i.e., the VGM. Figure 2 gives a "roadmap" of the steps which proceeded from the numerical and experimental studies described presently. In order to eliminate capillarity as a factor in the analysis, i.e. to show that inter- rather than intra-tow flow was the dominant factor, we first performed an analysis of capillary pressure in the material studied, Knytex 24 5×4.

Table 2. Equivalent permeabilities for various creeping flows.

	Velocity Equation	Permeability Constant
Darcy's law	$v = \frac{-K}{\mu} \cdot \frac{dP}{dx}$	K
Plane Poiseuille flow	$v_{ave} = -\frac{(b^2/3)}{\mu} \cdot \frac{dP}{dx}$	$b^2/3$
Circular Poiseuille flow	$v_{ave} = -\frac{(d^2/32)}{\mu} \cdot \frac{dP}{dx}$	$d^2/32$
Variable gap model	$v_{ave} = \frac{-\left(\frac{4}{3}\frac{a_1^2 a_2^2}{(a_1 + a_2)^2}\right)}{\mu} \cdot \frac{dP}{dx}$	$\frac{4}{3}\frac{a_1^2 a_2^2}{(a_1^2 + a_2^2)}$

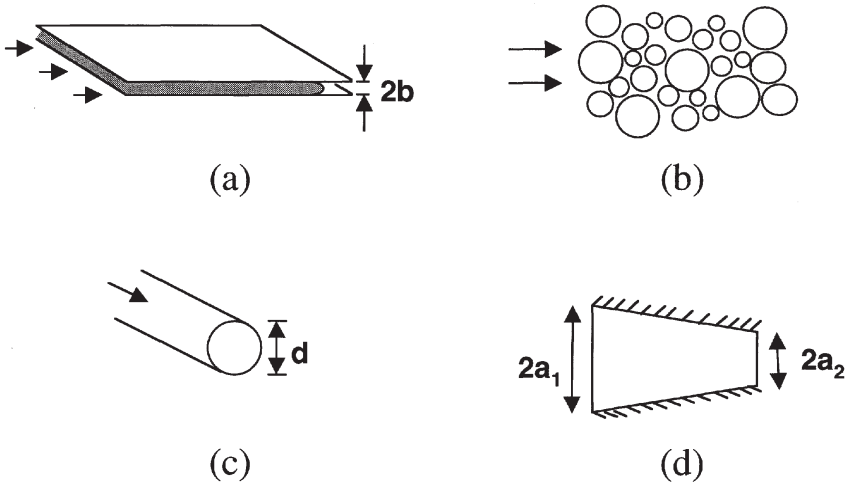

Figure 1. *Schematics of model flow domains, including: (a) planar Poiseuille flow, (b) Darcy flow, (c) circular Poiseuille flow, and (d) flow in channel of varying thickness.*

Capillarity: Analysis, Simulations and Experiments

DETERMINATION OF CAPILLARY PRESSURE

Capillary pressure is given by the classic Young-Laplace relation [e.g., Scheidegger (1974)] as

$$P^c = \frac{4 \cdot \sigma \cdot \cos(\psi)}{D_E} \tag{6}$$

where P^c is the capillary pressure, σ is the surface tension, ψ is the contact angle between the fluid and solid and D_E is the wetted diameter. D_E is equal to twice the gap distance for parallel plates and the diameter of the capillary tube in the case of a single tube (e.g., Chang et al., 1998).

The capillarity of a bundle of fibers can be derived using an equivalent wetted diameter (e.g., Lekakou and Bader, 1998)

$$D_E = \frac{8 \cdot r_f \cdot \varepsilon}{F \cdot (1 - \varepsilon)} \tag{7}$$

where r_f is the radius of a single fiber, ε is the porosity and F is a shape factor. Here, $F = 4$ for parallel flows and $F = 2$ for transverse flows. This expression assumes uniformly distributed cylinders. Skartsis et al. (1992c) improved the analytical capillary model by taking into account the structure and heterogene-

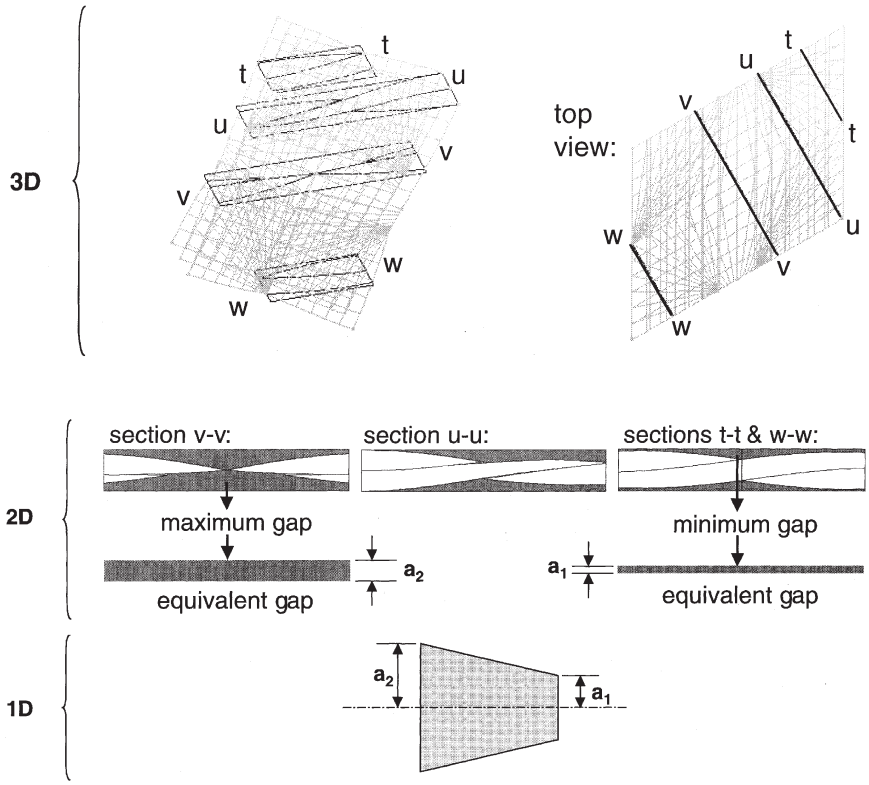

Figure 2. *Overview of the fabric model/gap model: two views of a 3D represenative cell obtained with the fabric model are shown ($\theta = 30°$). 2-D cross-sections ($\chi = 120°$) are shown including section v-v, which contains the maximum gap, cross-section u-u, an example of a cross-section with intermediate gaps, and sections t-t and w-w, which combine to form the cross-section that contains the minimum gap. The variable-gap model (1-D) is shown with dimensions a_2 and a_1 obtained from the equivalent maximum and minimum gap thicknesses, respectively.*

ity of the media, and reported agreement between analytical results and experiments.

CONTACT ANGLE MEASUREMENTS

The contact angle of corn oil (the fluid used in the fabric level experiments) with the surface of a glass fiber (17.2 μm diameter) was measured under an optical light microscope at room temperature. For fabric permeability experiments, both clear (unsaturated) and dyed (saturated) oils were used. Both clear and dyed oil/fiber contact angles were thus measured. Material properties on the fibers, tows, fabric and oil are given in Table 3.

A numerical method developed by Wagner (1990) was used to calculate the contact angle based upon the reduced droplet radius, reduced droplet length and fiber radius. This methodology was validated recently by Song et al. (1998) who showed that refinements in the contact angle measurement produced changes on the order of 10^{-1} degrees. A mean value of 20.11 degrees with standard deviation of 3.39 was found for the contact angle for clear oil; the dyed oil had a mean contact angle of 12.96 degrees with a standard deviation of 5.67.

Table 3. Material properties for Knytex 24-5×4 and corn oil, both clear and dyed.

Knytex 24-5×4 Plain-Weave Fabric	
Fiber composition	E-glass
Density of fiber material	2590 kg/m^3 (0.0935 lb/in^3)
Linear density of tows	207 yd/lb
Volume fraction of one layer of fabric	45.4%
Warp intratow volume fraction	78.6%
Weft intratow volume fraction	78.2%
Numbers of warp tows per inch	5
Numbers of weft tows per inch	4
Width of warp tows	5 mm
Width of weft tows	5 mm
Thickness of one layer of fabric	0.7366 mm
Number of glass fibrils per warp tow	4020
Number of glass fibrils per weft tow	4020
Diameter of a fibril	17.2 μm
Fabric lock angle	33 degrees
Clear Corn Oil	
Density	893 kg/m^3
Viscosity	0.040 kg/(m·s)
Dyed Corn Oil	
Density	892 kg/m^3
Viscosity	0.044 kg/(m·s)

TOW EXPERIMENTS

Single tows were carefully removed from the Knytex 24-5×4 fabric. The end of a tow was placed in a reservoir of oil; the oil level and tow were aligned horizontally. The thickness of the tow was calculated based upon measured volume fractions and geometry, and was found to be larger than the manufacturer's specifications.

Data reduction was accomplished via integration of Darcy's law, as

$$X^2 = \frac{2 \cdot K}{\mu} \cdot P \cdot t \tag{8}$$

where X is the flow progression length, K is the permeability, μ is the viscosity, P is the driving pressure and t is time. In a plot of flow progression length squared versus time, we obtained linear curves as shown in Figure 3, with

$$\text{slope} = \frac{2 \cdot K}{\mu} \cdot P \tag{9}$$

The capillary pressure was calculated to be 23 kPa, via Equation (11), using the experimental contact angle. Equivalent permeabilities were calculated from the slopes of the lines.

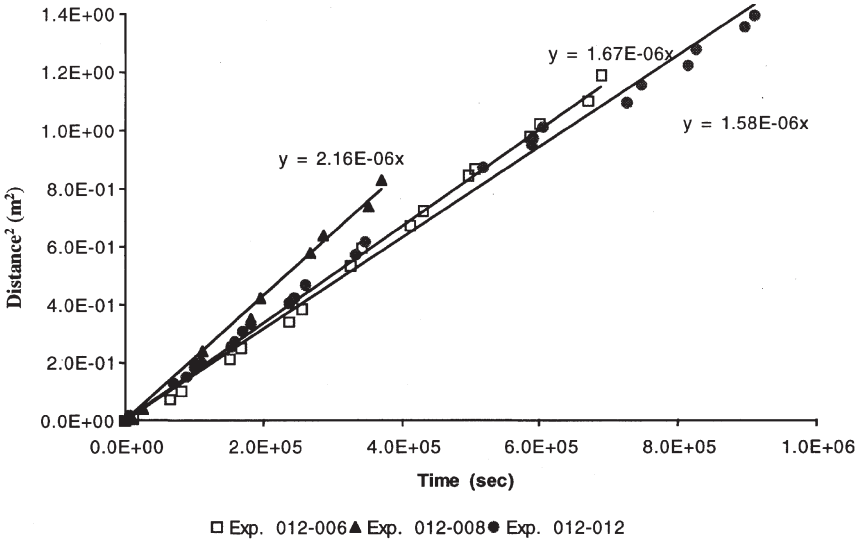

Figure 3. *Sample flow progression plot for single tow capillary wetting experiment, as (penetration distance)^2 versus time.*

The predicted permeabilities with different models and averaged experimental results are shown in Table 4. All predictions except Carman-Kozeny were an order of magnitude off from experimental findings.

COMPARISON WITH SIMULATIONS

Simulations were performed on prismatic sections, using the commercial CFD software FLUENT (Fluent Inc., v. 5.0, 1999). A momentum source representing the capillary pressure was added to the surface of the flow front. A Fortran algorithm tracing the flow front and adding a momentum source to necessary computational cells was incorporated into the software via a user-defined material subroutine. The fluid mechanics are summarized as follows. The momentum conservation equation in FLUENT takes the form

$$\frac{\partial}{\partial t}(\rho \cdot v_i) + \frac{\partial}{\partial x_j}(\rho \cdot v_i \cdot v_j) = -\frac{\partial P}{\partial x_i} + \frac{\partial \tau_{ij}}{\partial x_j} + \rho \cdot g_i + F_i \tag{10}$$

where F_i is the volume-averaged drag force, given by

$$F_i = -\frac{\mu}{K_i} \cdot v_i \tag{11}$$

Elements designated as porous cells (having capillarity) were checked to determine the volume fraction of oil in the cell and in the next cell in the flow direction. The flow front was located via addition of the momentum source to the conservation equation at the flow boundaries (the calculated capillary pressure was multiplied by the cross-sectional area of a single cell and the resulting surface force was applied to that cell in the flow direction as an equivalent body force). Comparison of simulations showed this approach to be equivalent to addition of a body force representing increased flow momentum due to capillarity.

A rectangular flow domain was created with two different sections. The upper half was assigned a permeability of 1×10^{-12} m^2 (suggested by experimental values of permeability from the intratow wetting experiments); the lower portion was

Table 4. Predicted and experimental intratow permeabilities.

	Axial Permeability	Transverse Permeability
Carman-Kozeny	2.6×10^{-12}	1.3×10^{-13}
Gebart (1992)	1.95×10^{-13}	2.93×10^{-14}
Cai and Berdichevsky (1993)	1.01×10^{-13}	5.91×10^{-14}
Berdichevsky and Cai (1993)	1.41×10^{-13}	3.51×10^{-14}
Experiments	1.56×10^{-12}	N/A

assigned a high permeability (gap region). Three types of simulations were run, with two different injection pressures. An equivalent permeability value of 8.3×10^{-8} m^2 was calculated using the gap thickness with Poiseuille flow (Table 2); this was the value implemented for the gap area in the simulation. The domains and the flow progression plots are shown in Figures 4 and 5. In both cases of injection pressure simulated, flow was gap-dominated, rather than tow-dominated. This is consistent with previous experimental and analytical data showing that the tow impregnation process is dominated by transverse impregnation rather than axial flow through the tow, e.g., Binétruy et al. (1998) who developed an analytical model for transverse tow impregnation. They observed experimentally that, except for very low velocities, transverse impregnation (rather than axial wicking) of tows dominates longitudinal intra-tow flow. Another observation which may be important in refining simulations is that the significance of the boundary conditions such as slip-no slip walls and surface tension diminished quickly with increasing injection pressure.

For the injection pressures of interest for low pressure permeation of Knytex 24 5×4, surface effects were thus found to be rather insignificant. Experimental injection pressures for the fabric permeability tests averaged 75 kPa; tow

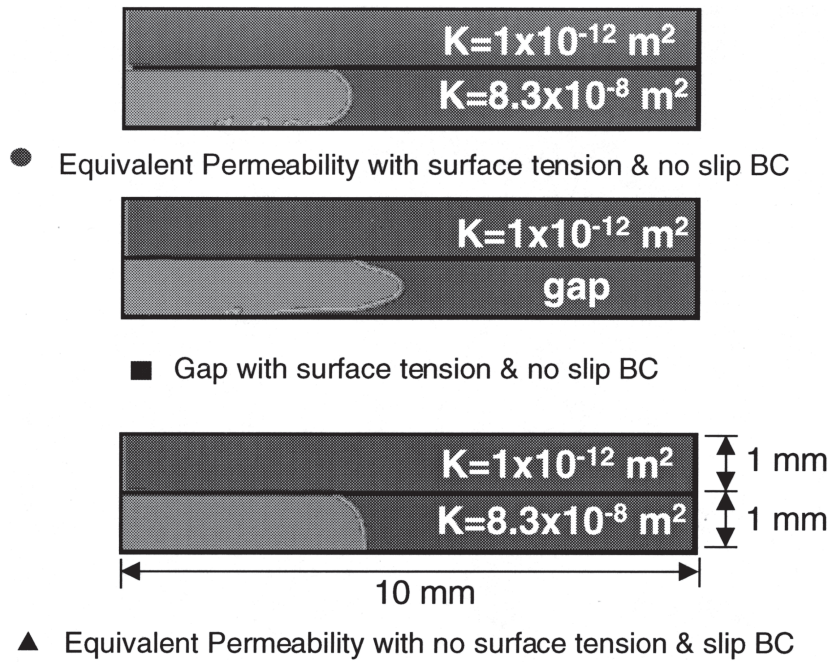

Figure 4. *Boundary conditions, permeabilities, and dimensions used in simulations whose results are reported in Figure 5. Flow fronts are shown at* $t = 4 \times 10^{-4}$ *sec.*

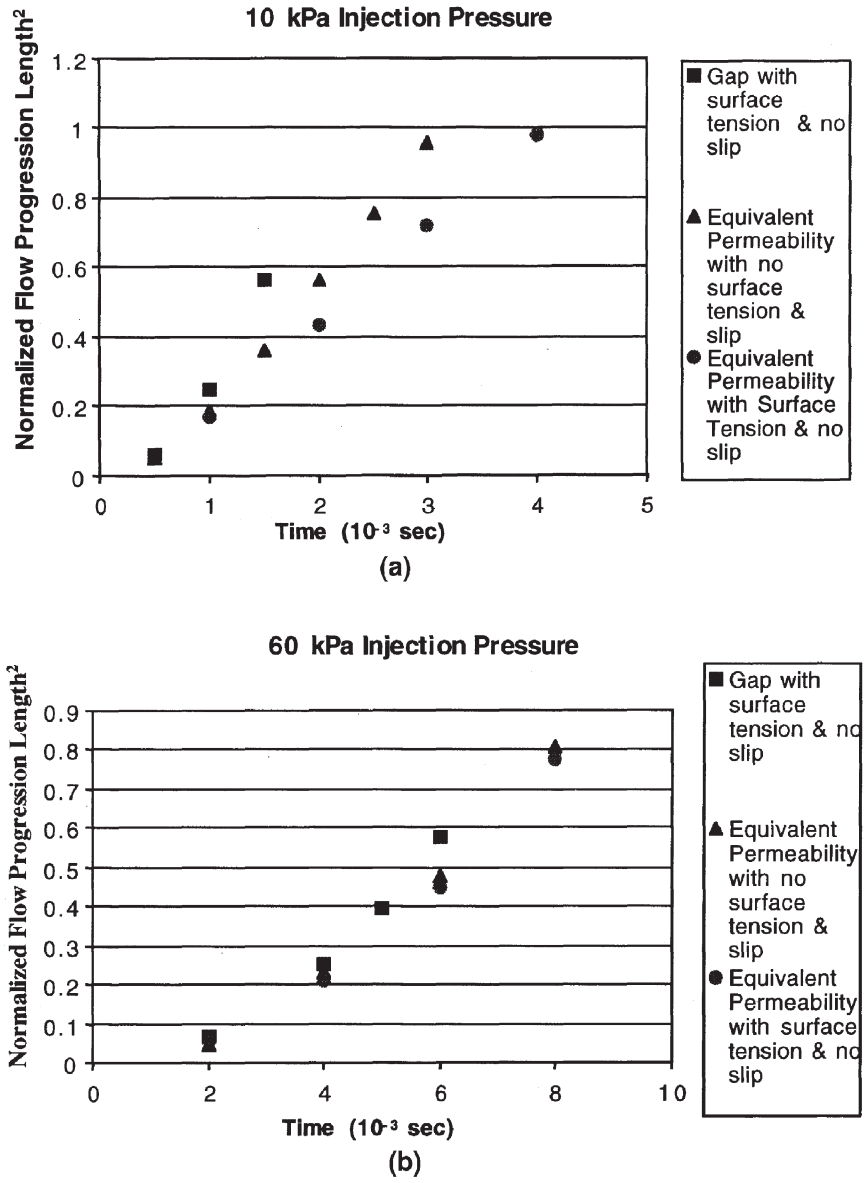

Figure 5. *Gap vs. intratow flow with (a) 10 kPa and (b) 60 kPa injection pressure.*

experiments resulted in calculated capillary pressures of approximately 23 kPa for the same material.

Tow Level Analyses: Application of the Variable Gap Model

Because of the dominance of gap flow for realistic processing cycles, a method for assessing the gap geometry using the fabric model was developed. As shown in Figure 2, the model accounted only for flow in the gaps of the fabric. Per the VGM equation (Table 2), permeability is sensitive to narrow sections of a flow channel. Thus, using a Poiseuille approach with a single gap width would not sufficiently capture the tortuosity of flow in a fabric. This is supported by evidence of the failure of simple volume fraction calculations to correct permeabilities from the unsheared configuration to predict permeabilities in sheared configurations. Though volume fraction certainly increases with shear, changes in the microarchitecture have a more significant effect, i.e., the placement of tows (barriers) is more significant than their volume fraction for this material and shear range.

The fabric model developed as Part I of this work (Dungan et al., 2001) was used to develop expressions for equivalent gap thickness for arbitrary sections. The gap between two layers of fabric was isolated directly from the fabric model, whereupon gap area was found. Two extreme cases were considered, suggested by the characterizations of the effects of nesting in Part I—the cases of no nesting and maximum nesting. Possible effects from deflections of the mold top were ruled out for the experiment via finite element analysis (Dungan, 2000). The maximum deflection at the center of the mold top was found to be 0.05% of the standard mold cavity thickness, so racetracking between the bottom of the mold top and the top of the fabric reinforcements was not considered.

In the case of no nesting, shown schematically as Figure 6(a), the gap areas between the tows and a flat surface were measured for both the upper surface of the tows and their lower surface. The number of cross-sections taken for each shear angle (σ)-cross-section angle (χ) pair varied between 2 and 16. In most cases, cross-sections were taken at just 2 strategic locations: the cross-section passing through the middle of the symmetric cross-section, and the cross-section made up of two incomplete cross-sections of the same length, i.e., the cross-section whose two pieces were located in the middle of the range of incomplete cross-sections. Those locations were identified as representing minimum and maximum gaps, for any shear angle (θ)-cross-section angle (χ) pair.

In the case of no nesting, shown schematically as Figure 6(b), the gaps between two fabric layers offset by $S_a/2$ in the warp direction and $S_b/2$ in the weft direction over an area of one representative cell were measured. For the maximum nesting case, no trend was apparent from pictures of cross-sections or from initial measurements. The number of cross-sections taken for each shear angle (θ)-cross-sec-

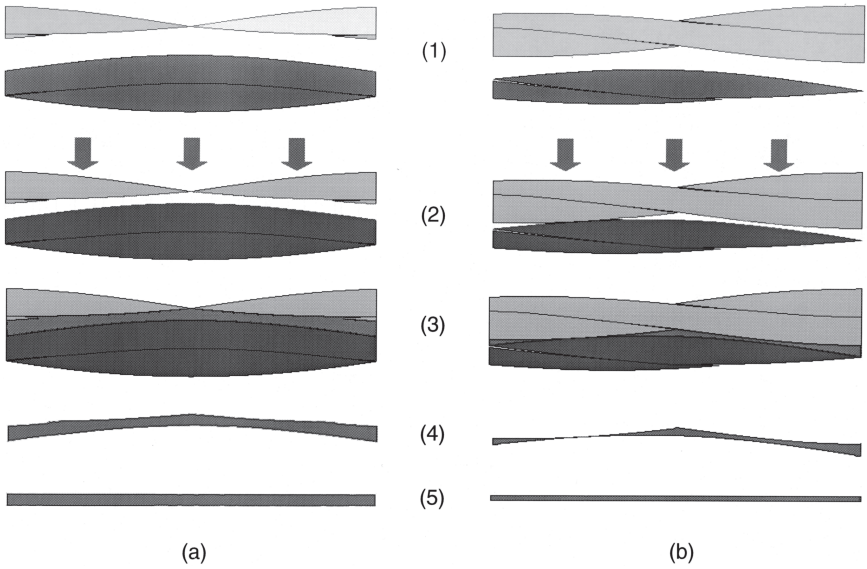

Figure 6. *Cross-section through 2 layers of fabric. Examples: (a) maximum gap for θ = 15°, χ = 110°, (b) minimum gap for θ = 15°, χ = 110°. Configurations shown are (1) no nesting, (2) nesting with thickness reduction, (3) gap highlighted, (4) gaps isolated, and (5) rectangle with equivalent thickness.*

tion angle (χ) pair varied between 5 and 9. For each cross-section, the gap area was measured for each of the 4 cases shown in Part I [Figure 23(a) in Dungan et al., 2001].

For each shear angle (θ)-cross-section angle (χ) pair, then, equivalent gap thicknesses were determined for two cases: the minimum and maximum gap thicknesses. These were then entered into the VGM equation to determine the effective permeability for each pair.

APPLICATION OF THE VARIABLE GAP MODEL TO DETERMINATION OF FABRIC PERMEABILITIES

In the experiments described in Dungan et al. (1999) and Dungan et al. (2001), the warp tows were rotated CCW to produce fabric shear; weft tows were fixed parallel to the *y* axis for all experiments. Figures 7 and 8 give the notation for the experiments and subsequent analysis. Lines passing through the diagonals of unit cells are located at CCW rotations of α_1 and α_2, respectively, from the warp tows. Figure 7 shows the location of these for the unsheared configuration, along with principal flow angle η; Figure 8 shows the locations of these angles for a sheared configuration.

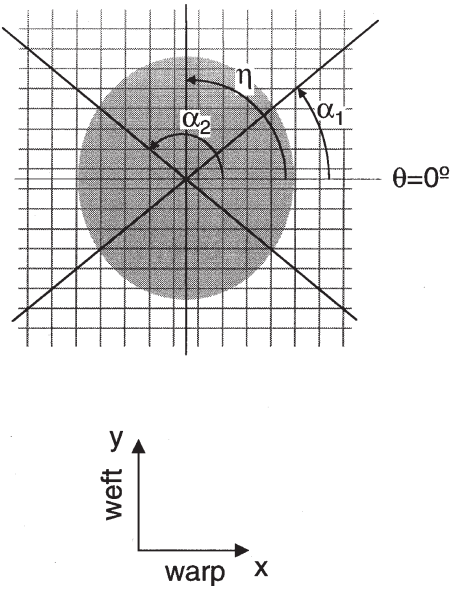

Figure 7. *Angle notation for experimental data for an unsheared fabric case. The shaded area represents a typical experimental flow front shape.*

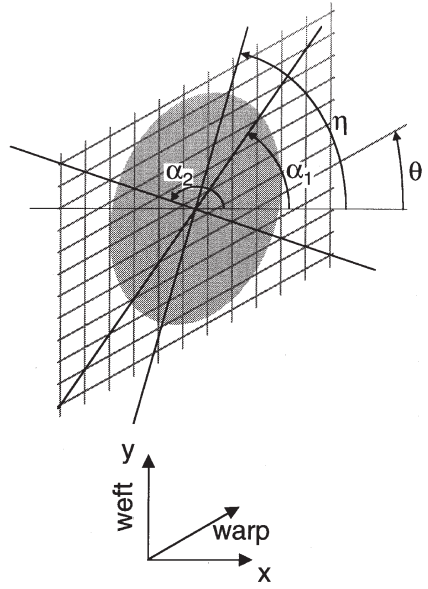

Figure 8. *Angle notation for experimental data for a sheared fabric case. The shaded area represents a typical experimental flow front shape.*

For comparison with the calculated permeabilities, angles γ were defined as shown in Figure 9. These angle definitions were convenient, since they represented the preferred flow directions (discussed presently). Note that nothing in the following analyses assumes the location of the principal flow direction (η); it is determined via the permeability gap calculations. Thus, unlike trigonometric or semi-empirical models (e.g., Lai and Young, 1997), the principal flow angle was not assumed *a priori* to be related to any material or shear parameter.

Data Reduction: Modeling of Experimental Flow Fronts

An algorithm was developed to find the best-fitting ellipse for a set of calculated permeability data obtained with the variable gap model. A general ellipse centered at the origin is shown in Figure 10, defined as

$$\sqrt{((-A)-x)^2+((-B)-y)^2}+\sqrt{(A-x)^2+(B-y)^2}=D \qquad (12)$$

where (x,y) is a point on the ellipse, A is the distance between either focus and the y axis, and B is the distance between either focus and the x axis. D is the sum of the

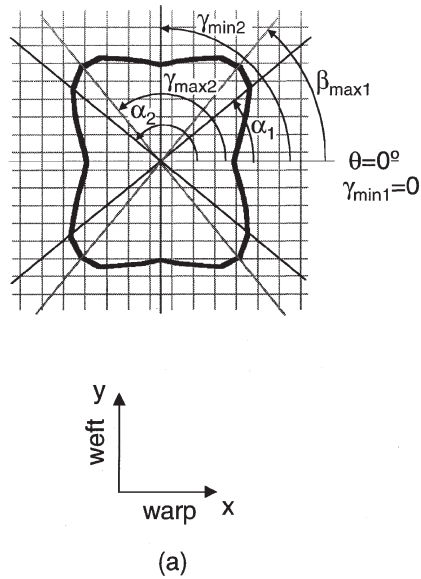

Figure 9. *Overview of angle notation for calculated data: (a) unsheared fabric case and (b) sheared fabric case. The curves represent typical calculated permeability data based on the variable gap model.*

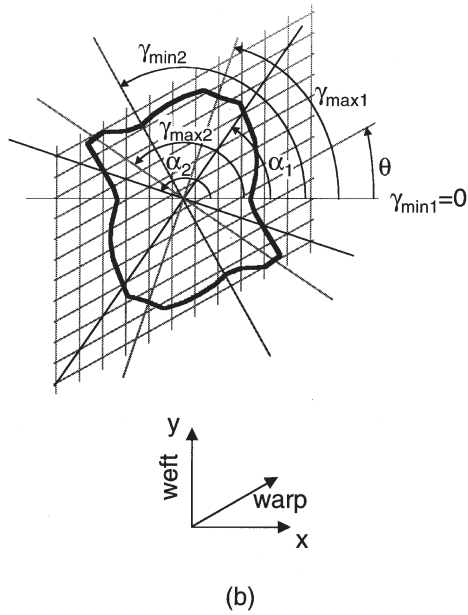

Figure 9 (continued). *Overview of angle notation for calculated data: (a) unsheared fabric case and (b) sheared fabric case. The curves represent typical calculated permeability data based on the variable gap model.*

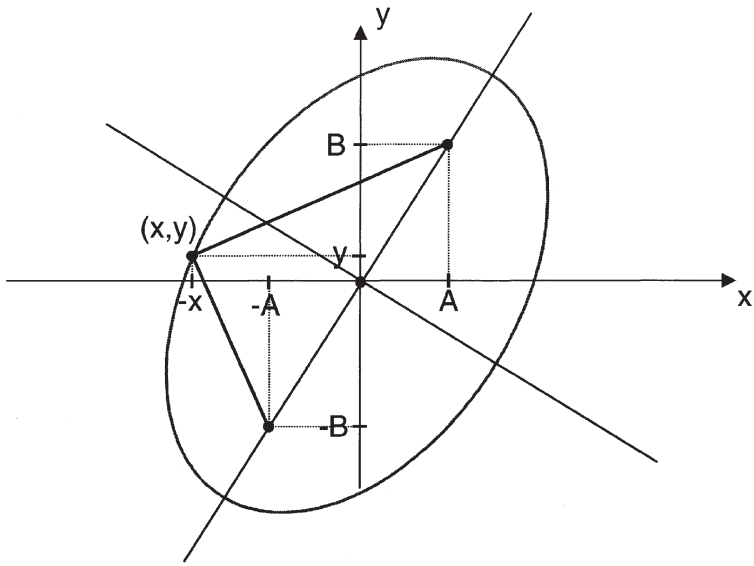

Figure 10. *Description of a general ellipse centered at the origin.*

distances between any point on the ellipse and the two foci. For any angle χ (measured counterclockwise from the x axis),

$$y = x\tan(\chi) \tag{13}$$

and

$$y = \pm\sqrt{\frac{D^2(-4A^2 - 4B^2 + D^2)}{-16A^2 + 4D^2 - 32AB\tan(\chi) - 16B^2(\tan(\chi))^2 + 4D^2(\tan(\chi))^2}} \tag{14}$$

Since tan(90°) tends to infinity, $\chi = 90°$ was treated as a special case with $x = 0$ and

$$y = \pm\sqrt{\frac{D^2(-4A^2 - 4B^2 + D^2)}{-16B^2 + 4D^2}} \tag{15}$$

A program was written to find the ellipse minimizing an error measure defined as

$$\text{error} = \sum_{i=1}^{N}\sqrt{(x_i - P_i)^2 + (y_i - Q_i)^2} \tag{16}$$

for a given set of N data points (P_i, Q_i) and points (x_i, y_i) on the ellipse at corresponding angles χ_i. An additional constraint was introduced in order to ensure that the area of the ellipse was conserved. The area of the polygon defined by the data points (P_i, Q_i) was calculated using

$$\text{area} = \sum_{i=1}^{N} 2\tan\left(\frac{\chi_{i+1} - \chi_i}{2}\right)\left[\left(\frac{x_{i+1} + x_i}{2}\right)^2 + \left(\frac{y_{i+1} + y_i}{2}\right)^2\right] \tag{17}$$

and the area of the best-fit ellipse was constrained to that area. A schematic of this error calculation for an actual case ($\chi = 20°$ and $\theta = 30°$) is shown as Figure 11.

Comparison of Theory and Experiment: Prediction of Permeability Using the Variable Gap Model

Three cases were examined using the variable gap model to predict permeability: fabric-to-fabric with maximum nesting, fabric-to-fabric with minimum nesting, and fabric-to-flat surface. These three conditions represent the extremes of situations occurring in a real mold, with the flat surface representing the mold top or bottom. The corresponding permeabilities, along with the experimental saturated and unsaturated permeabilities, are shown in Figures 12, 13 and 14, for 0°, 15° and 30° shear, respectively. In all cases, the calculated permeability curves (based on

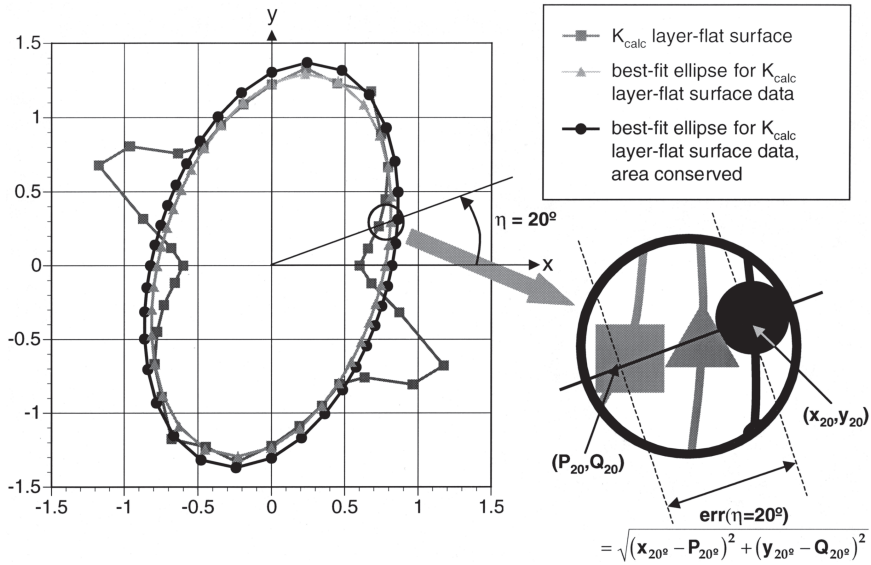

Figure 11. *Fitting of calculated permeabilities with ellipse. This example shows the calculated permeabilities obtained for a shear angle of 30 degrees, based on the gaps between one layer of fabric and a flat surface. The enlarged area shows the parameters involved in the calculation of error for the data at* $\eta = 20°$ *as an example. The error for the data points at* $\eta = 20°$ *is* $err(\eta = 20°) = \sqrt{(x_{20°} - P_{20°})^2 + (y_{20°} - Q_{20°})^2}$.

point-by-point calculation of permeability for a χ–θ pair) were irregular (i.e., not elliptical); this is discussed in the next section. The minimum permeability in each case was for the fabric-fabric maximum nesting; the maximum permeability was always associated with the fabric-fabric minimum nesting. In all cases, the fabric-flat surface calculations produced intermediate values of permeability. Also, in all cases, the experimental permeabilities were bounded by these predictions.

Comparison of Theory and Experiment: Prediction of Principal Directions Using the Variable Gap Model

Flow was significantly impeded when oriented at 90° to tows, and enhanced when normal to planes cutting opposite corners of representative cells. This can be readily seen by the "lobes" in the calculated permeability curves using this 3D fabric/1D fluid modeling approach. Maximum flow occurred across planes defined by the critical angles. Thus, the maximum flow angles were $\alpha_1 \pm 90°$ and $\alpha_2 \pm 90°$ and denoted γ_{max1} and γ_{max2}, respectively, as

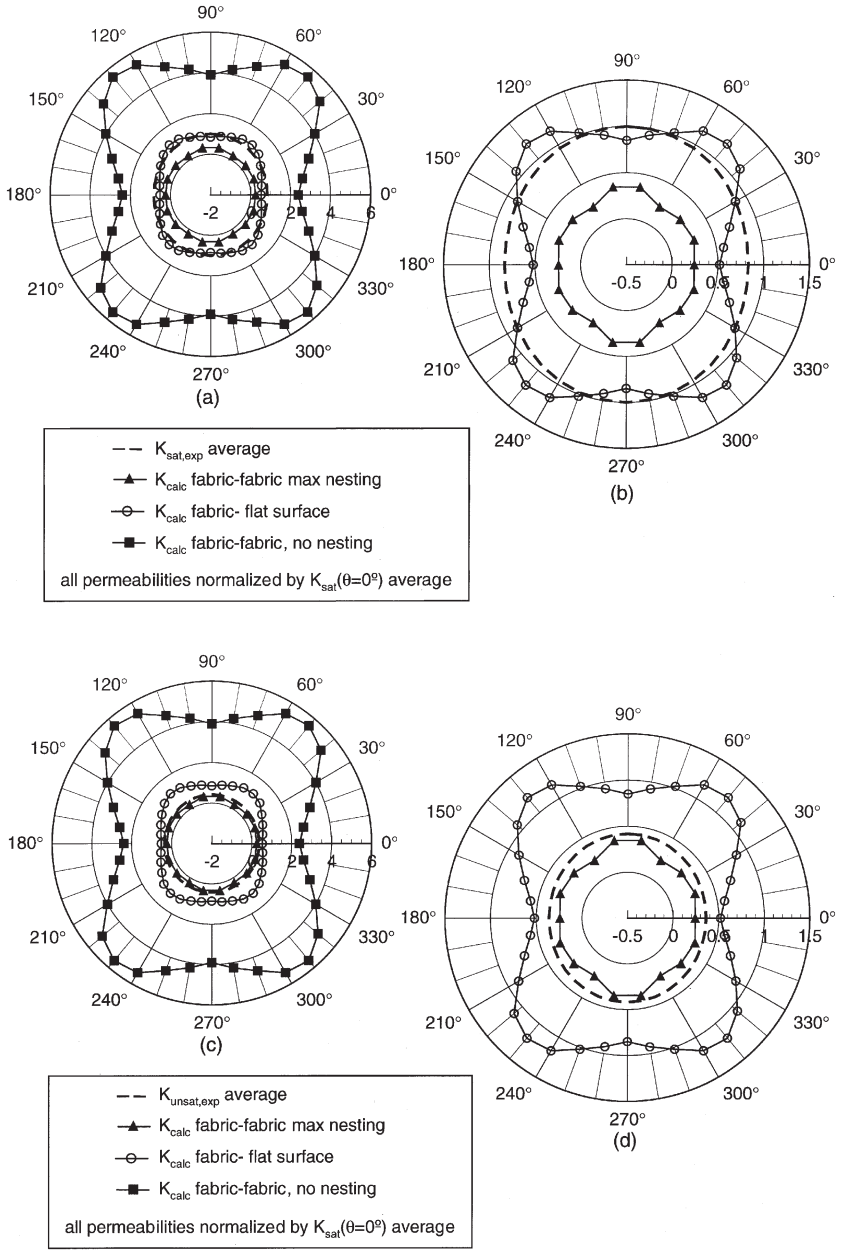

Figure 12. *Experimental and gap-based calculated permeabilities for unsheared fabric. All data are normalized with respect to K_{1exp} ($\theta = 0°$). (a) and (b) give all saturated curves and a close-up of saturated curves, respectively; (c) and (d) give results for the unsaturated cases.*

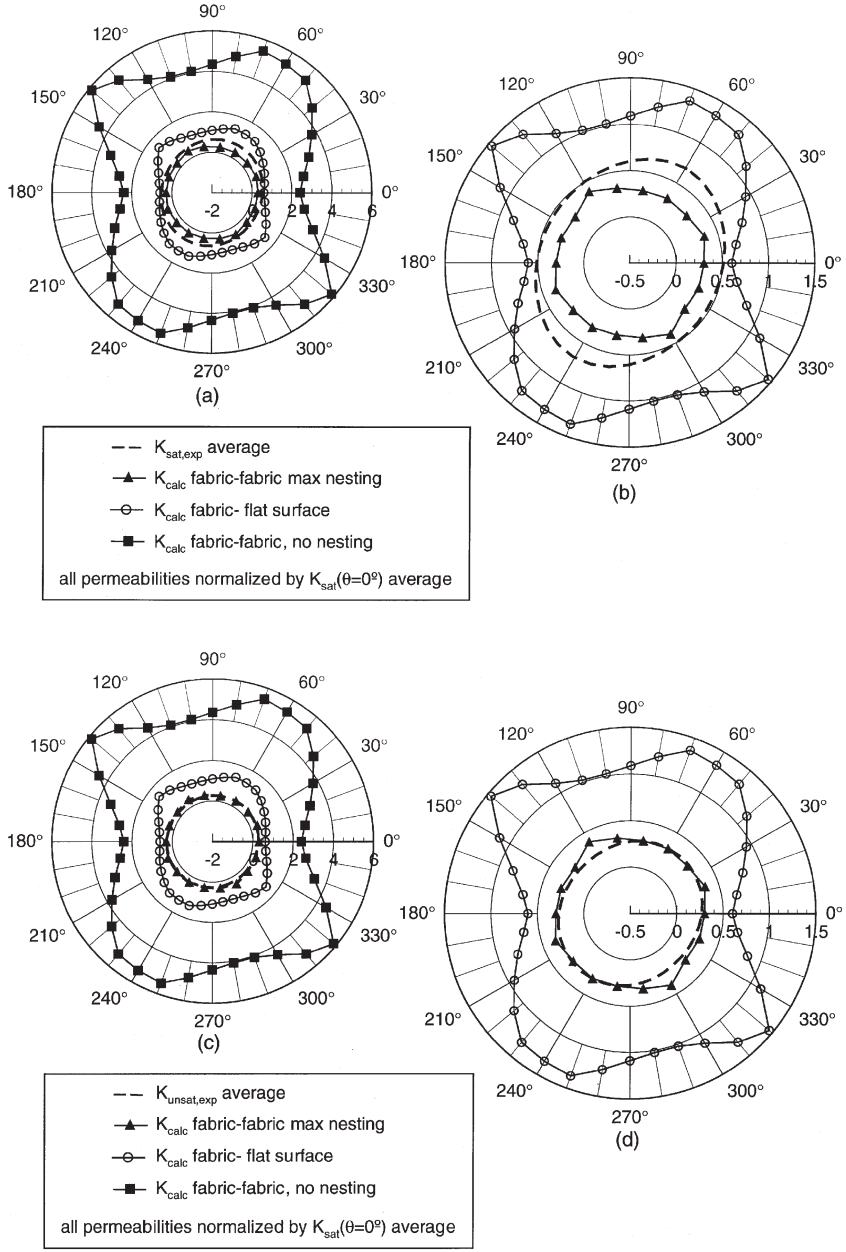

Figure 13. *Experimental and gap-based calculated permeabilities for* $\theta = 15°$. *All data are normalized with respect to* $K_{1exp,sat}$ ($\theta = 0°$). *(a) and (b) give all saturated curves and a close-up of saturated curves, respectively; (c) and (d) give results for the unsaturated cases.*

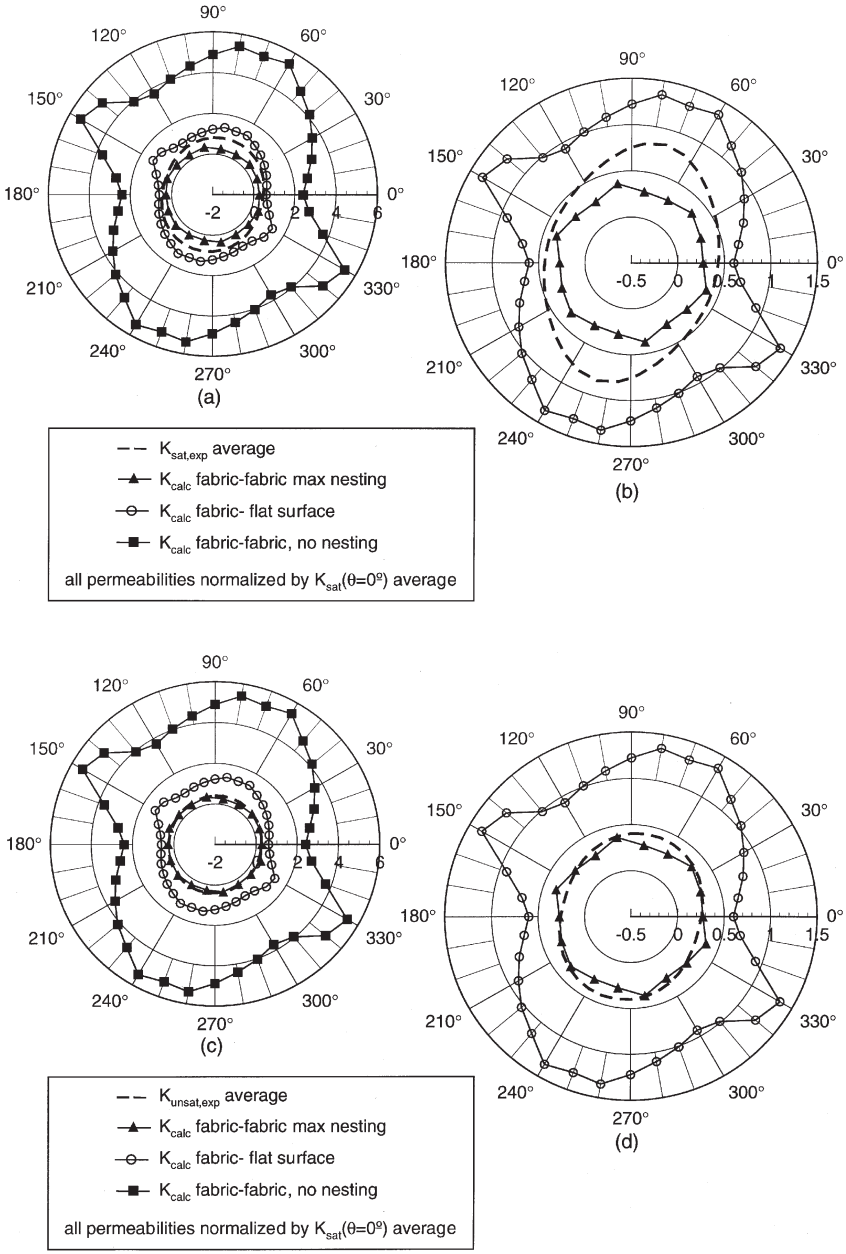

Figure 14. *Experimental and gap-based calculated permeabilities for* $\theta = 30°$. *All data are normalized with respect to* $K_{1exp,sat}$ ($\theta = 0°$). *(a) and (b) give all saturated curves and a close-up of saturated curves, respectively; (c) and (d) give results for the unsaturated cases.*

$$\gamma_{max1} = \alpha_2 \pm 90° \tag{18}$$

$$\gamma_{max2} = \alpha_1 \pm 90° \tag{19}$$

These are as shown in Figure 9. The minimum flow angles occurred across the warp and weft directions, i.e., $\theta \pm 90°$ and [0°,180°] (since the weft tows were fixed at 0°). These minimum angles γ_{min1} and γ_{min2}, were defined as

$$\gamma_{min1} = 0°, 180° \tag{20}$$

$$\gamma_{min2} = \theta \pm 90° \tag{21}$$

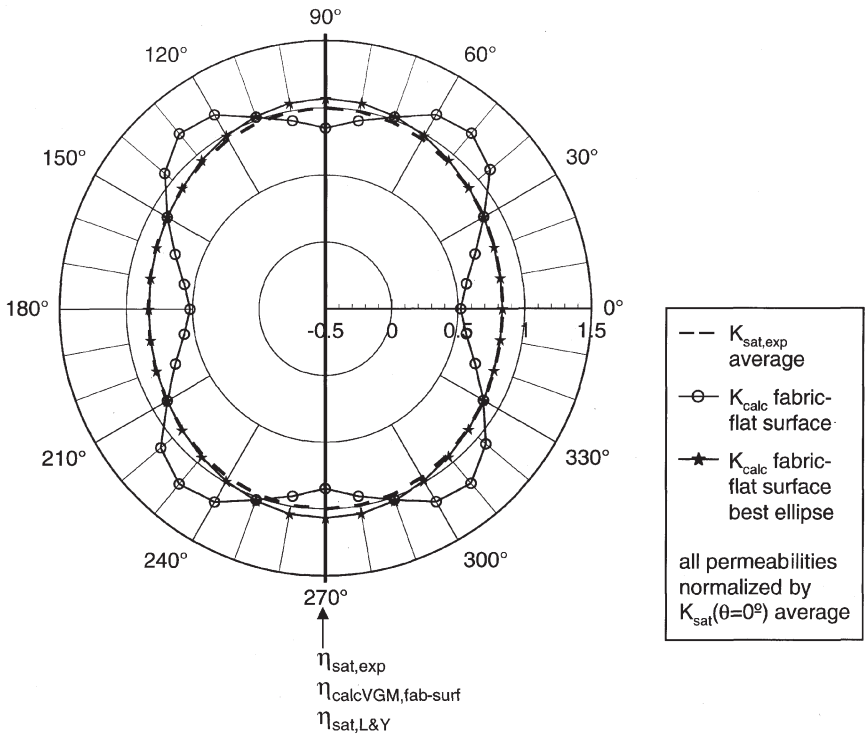

Figure 15. *Comparison of principal flow directions for unsheared fabric. The principal flow direction obtained from saturated experimental data, $\eta_{sat,exp}$, is compared to the principal flow direction based on the variable-gap model, η_{VGM}, which is the direction of the major axis of the best-fit ellipse for the calculated permeabilities obtained with the variable-gap model (based on gaps between one layer of fabric and a flat surface), and the principal flow direction obtained with Lai and Young's (1997) method (with a fitting parameter* m *equal to 0.83).*

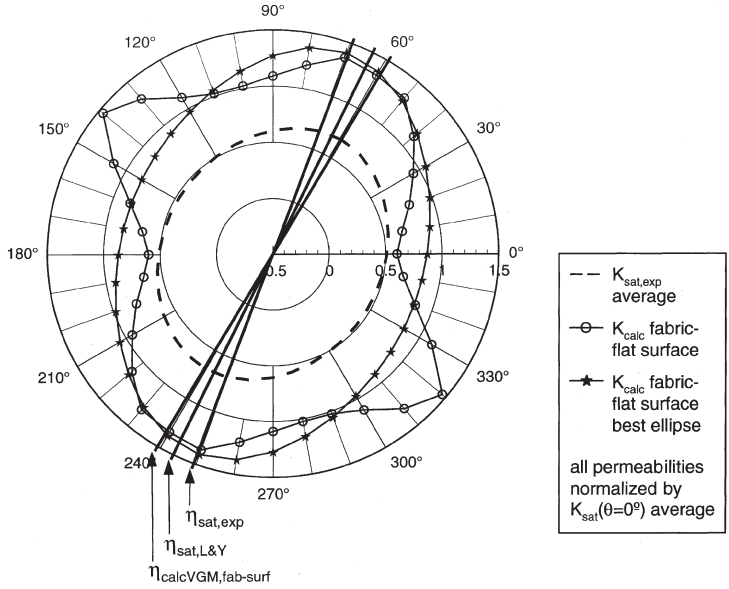

Figure 16. *Comparison of principal flow directions for θ = 15°, with parameters as defined in Figure 15.*

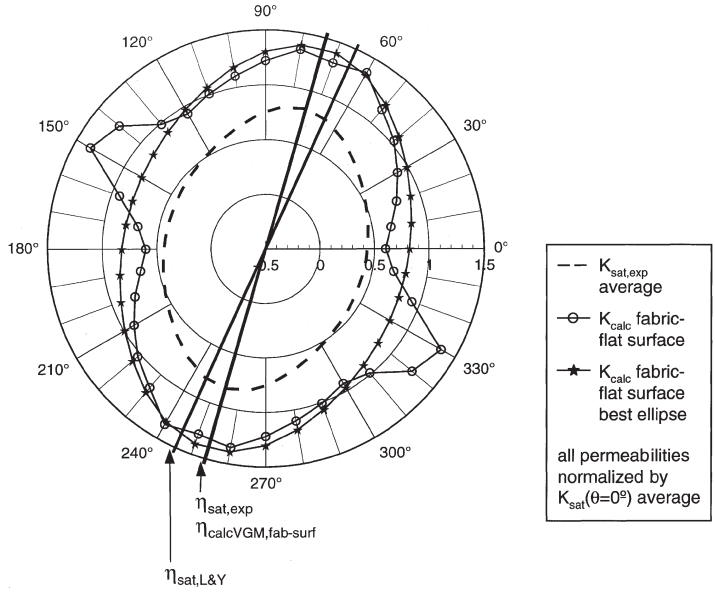

Figure 17. *Comparison of principal flow directions for θ = 30°, with parameters as defined in Figure 15.*

Table 5. Comparison of principal flow directions from experiments, calculations, and Lai and Young's model.

Shear Angle (degrees)	15	30
$\eta_{exp,unsat}$ (degrees)	47.4	74.2
$\eta_{exp,sat}$ (degrees)	59.2	74.0
η_{calc} (degrees) (% error relative to $\eta_{exp,sat}$)	69.4 (17.2)	73.8 (0.270)
$\eta_{Lai\&Young,unsat,m=1.0}$ (degrees) (% error relative to $\eta_{exp,unsat}$)	60.2 (27.0)	63.6 (14.3)
$\eta_{Lai\&Young,sat,m=0.83}$ (degrees) (% error relative to $\eta_{exp,sat}$)	63.7 (7.60)	65.4 (11.6)

Note: All the principal flow angles are 90 degrees for unsheared fabric.

The "cloverleaf" patterns exhibited by the permeability data obtained with the variable gap model as shown in Figures 12–14 result from these preferred directions, which are artifacts of the 1D analysis performed for the fluids calculation. The flow favors the direction $\alpha_2 \pm 90°$ over $\alpha_1 \pm 90°$ for shear angles other than zero because the plane across which the flow proceeds makes a larger angle with the warp and the weft for the $\alpha_2 \pm 90°$ case than for the $\alpha_1 \pm 90°$ case. Flow in the minimum flow direction (0°) is the most restricted because it hits the weft tows "dead-on"; the remaining (warp) tows for the Knytex 24 5×4 have no gaps between them (see Dungan et al., 2001, Figure 1), resulting in a low channel area for the normal flow.

The predictions of principal flow angles (η) are shown in Figures 15–17, for 0°, 15° and 30° shear, respectively. These principal angles were determined by location of the major axis of a best-fit ellipse through all calculated 1D permeabilities,

Table 6. Critical flow directions based on the relative orientation of the warp and weft tows.

Shear Angle (degrees)	0	15	30
γ_{max1} (degrees)	51.8	61.3	71.6
γ_{max2} (degrees)	128	137	146
γ_{min1} (degrees)	0	0	0
γ_{min2} (degrees)	90	105	120

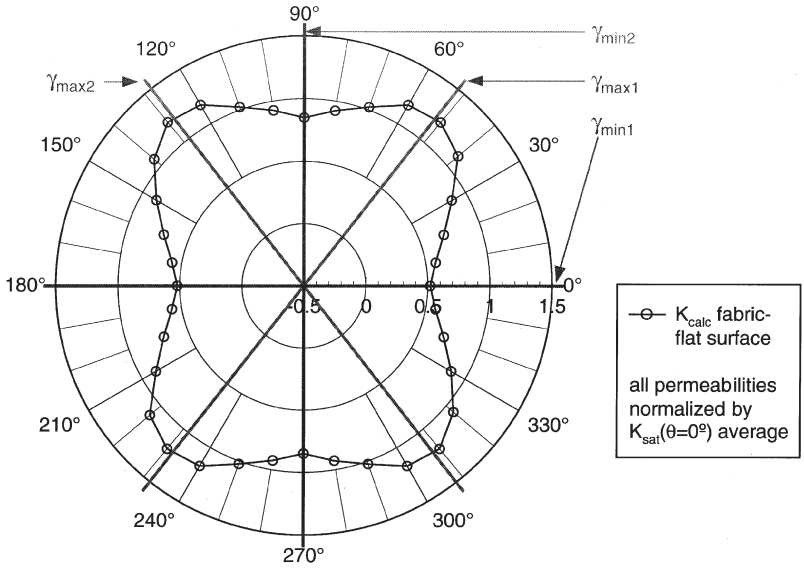

Figure 18. *Critical flow directions based on the relative orientation of the warp and weft tows for unsheared fabric shown with calculated permeabilities for θ = 0° obtained with the variable-gap model (based on gaps between a layer of fabric and a flat surface).*

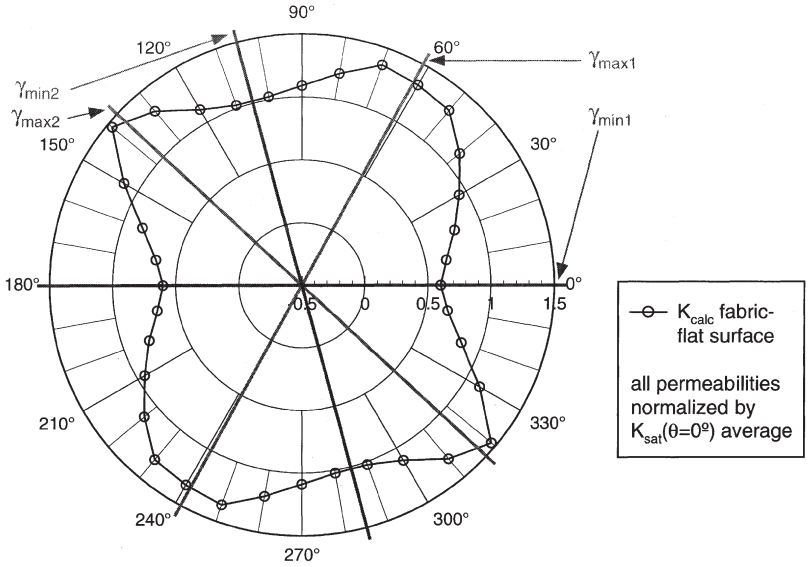

Figure 19. *Critical flow directions based on the relative orientation of the warp and weft tows for θ = 15° shown with calculated permeabilities for θ = 15° obtained with the variable-gap model (based on gaps between a layer of fabric and a flat surface).*

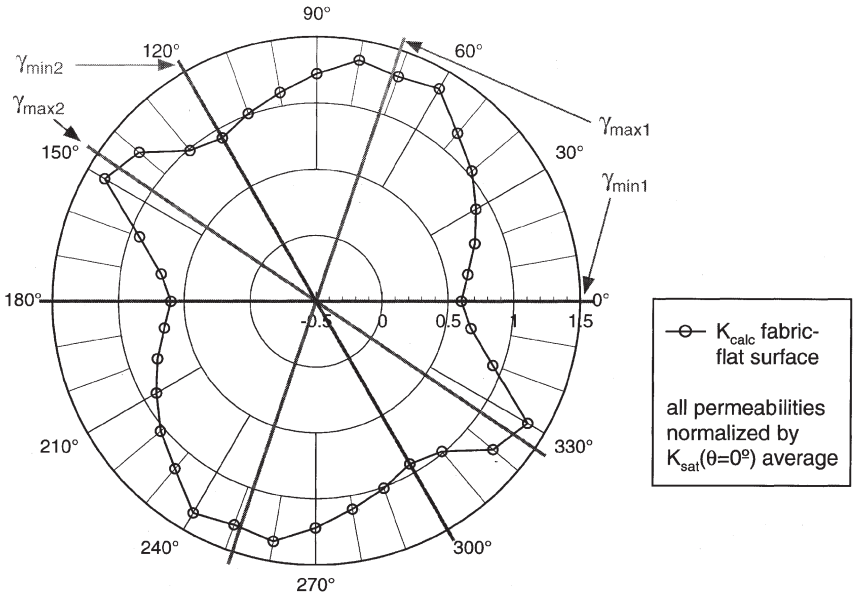

Figure 20. *Critical flow directions based on the relative orientation of the warp and weft tows for θ = 30° shown with calculated permeabilities for θ = 30° obtained with the variable-gap model (based on gaps between a layer of fabric and a flat surface).*

as shown in Figure 11. On all of these plots, comparison is made with the empirical model of Lai and Young (1997). Values are summarized in Table 5, with critical flow angles based on relative angles of warp and weft given in Table 6. For the unsheared and 30° sheared cases, the VGM, in concert with the fabric model, provided a superior representation even than the empirical model of Lai and Young (1997). The result was also close to the experimental result for the 15° case.

In order to validate our assumption concerning the location of the minimum and maximum flow angles, plots of these values were made for each shear angle, as shown in Figures 18–20. As seen in these plots and in Table 6, which contains numerical values, the minima and maxima do arise quite close to the locations described above.

DISCUSSION AND FUTURE WORK

Generation of a 3D fabric model was used to describe a simple flow channel in an unbalanced plain-woven fabric. In all cases studied for saturated flow, use of the very detailed 3D model to generate information for the 1D flow model offered bounds on permeabilities when nesting was accounted for, provided good predic-

tion of principal flow directions, especially close to the lock angle of the fabric, and offered a superior prediction than even an empirical model requiring experiments to pre-determine permeabilities in both sheared and unsheared configurations. In the model developed here, only the fabric architecture and material properties were used, offering an extremely efficient tool for prediction of flow fronts.

Several factors commonly blamed for disagreements in measured fabric permeabilities by different investigators were examined in detail in the present studies. The presence of Poiseuille flow between the fabric layers and the top of the mold was obvious during the 7-layer experiments, producing flow fronts which were qualitatively dissimilar to those in experiments involving more layers, for the same mold dimensions. Moreover, experimental permeabilities for these 7-layer cases were an order of magnitude greater than for eight layers in the same mold. These differences were large enough that only very few data were taken. Numerical simulations of mold top deflections showed that they were negligibly small in affecting the cavity geometry of our experiments. Also, capillary effects were shown to be small, resulting in their omission in the fluid mechanics model.

The higher values of permeability in the saturated versus unsaturated experiments reported here (see Tables 7 and 8) have been supported by some workers. Because of the small influence of capillary wetting and the resulting low estimates of intratow permeability for the experimental conditions, we did not expect to see higher permeability in the unsaturated materials due to wicking. However, the significantly larger values of permeability observed for saturated materials provide even greater justification for elimination of capillary forces as a factor, since wicking would produce greater permeability in the unsaturated condition. For the 0°, 15° and 30° cases, the saturated principal permeabilities were approximately 140%, 120% and 100% higher (K_1) and 130%, 110% and 80% higher (K_2) than the analogous unsaturated cases. These differences were exceeded, however, by differences in the predicted permeabilities for the extremes of nesting. For the 0°, 15° and 30° cases, predicted permeabilities (VGM, identical for both saturated and unsaturated conditions), principal permeabilities were approximately 17, 15, and 16 times higher (K_1) and 14, 13, and 12 times higher (K_2) for the perfectly non-nested than for the perfectly nested cases. Thus, though greater permeabilities for saturated than unsaturated conditions were observed here, in agreement with other workers' results, these differences were dwarfed by the order-of-magnitude differences predicted between the bounds when interlayer geometry was considered.

We hypothesize that the enhanced permeability in the saturated materials arises from reduction in roughness of fibers and fiber bundles due to the coating with oil. As with reduction of friction factors in smooth pipes, we suspect that the oil coating significantly enhances flow due to pre-wetting. It is unlikely that tow penetration during injection in unsaturated experiments strongly affects flow by reducing permeability, simply because calculated permeabilities show that tow penetration and gap flow, for the experimental conditions, occurred on different timescales.

Table 7. Numerical values of permeabilities for saturated flow.*

Shear Angle (degrees)	0	15	30
Average experimental K_1 ($*10^{-10}$ m^2)	15.1	10.4	12.6
K_1 based on transformed unsheared K's without V_f correction ($*10^{-10}$ m^2)	15.1	17.6 (69.2)	20.9 (65.9)
K_1 based on transformed unsheared K's with V_f correction ($*10^{-10}$ m^2)	15.1	15.3 (47.1)	11.4 (9.52)
K_{1calc} with VGM (max nesting) ($*10^{-10}$ m^2)	4.50 (70.2)	5.80 (44.2)	5.31 (57.9)
K_{1calc} with VGM (layer/flat surface) ($*10^{-10}$ m^2)	16.1 (6.62)	21.3 (105)	21.2 (68.3)
K_{1calc} with VGM (4 layers in mold, no nesting) ($*10^{-10}$ m^2)	74.3 (392)	85.9 (726)	84.6 (571)
Average experimental K_2 ($*10^{-10}$ m^2)	12.6	7.17	6.38
K_2 based on transformed unsheared K's without V_f correction ($*10^{-10}$ m^2)	12.6	10.1 (40.9)	6.84 (7.21)
K_2 based on transformed unsheared K's with V_f correction ($*10^{-10}$ m^2)	12.6	8.76 (22.2)	3.72 (41.7)
K_{2calc} with VGM (max nesting) ($*10^{-10}$ m^2)	4.01 (68.2)	3.96 (43.8)	4.05 (36.5)
K_{2calc} with VGM (layer/flat surface) ($*10^{-10}$ m^2)	12.6 (0.0)	12.6 (23.8)	12.1 (89.6)
K_{2calc} with VGM (4 layers in mold, nesting) ($*10^{-10}$ m^2)	57.7 (358)	50.4 (603)	48.3 (657)

*Experimental values, values calculated with the transformation of unsheared permeabilities with and without volume fraction correction, and values calculated with variable gap model for all 3 cases investigated are shown. Percent errors with respect to corresponding experimental value are given in parentheses.

Thus, by the time the fluid penetrated the tows, the experiment was likely to be over (with experimental flow fronts measured at short time intervals, of approximately 2–15 seconds after injection was initiated).

As discussed in Part I of this work (Dungan et al., 2001), the 3D model predicts no greater nesting effect for different shear angles. Note that in our model, compaction was not considered, though tow volume fractions were initially well below theoretical maxima (~78% intratow V_f, per our measurements). Practically, one might expect greater tendency to nest for higher shear angles since interlayer sliding would naturally occur as stacks became sheared; this interlayer slip would be diminished as layers became nested. Our experiments involved extremely careful placement of both unsheared and sheared layers. However, in placement of sheared layers, more adjustment was required to assure each layer's tows were properly oriented in the mold than for the unsheared layers. When the sheared layers become nested, they become both more resistant to further transverse movement (since the nesting acts as a weak locking mechanism in the dry material), and moreover, the material needs no further adjustment since it is aligned with the pre-

Table 8. Numerical values of permeabilities for unsaturated flow.*

Shear Angle (degrees)	0	15	30
Average experimental K_1 ($*10^{-10}$ m^2)	6.32	4.76	6.24
K_1 based on transformed unsheared K's without V_f correction ($*10^{-10}$ m^2)	6.32	7.46 (56.7)	8.85 (41.8)
K_1 based on transformed unsheared K's with V_f correction ($*10^{-10}$ m^2)	6.32	6.49 (36.3)	4.81 (22.9)
K_{1calc} with VGM (max nesting) ($*10^{-10}$ m^2)	4.50 (28.8)	5.80 (21.8)	5.31 (14.9)
K_{1calc} with VGM (layer/flat surface) ($*10^{-10}$ m^2)	16.1 (155)	21.3 (347)	21.2 (236)
K_{1calc} with VGM (4 layers in mold, no nesting) ($*10^{-10}$ m^2)	74.3 (1080)	85.9 (1700)	84.6 (1260)
Average experimental K_2 ($*10^{-10}$ m^2)	5.45	3.36	3.61
K_2 based on transformed unsheared K's without V_f correction ($*10^{-10}$ m^2)	5.45	4.30 (28.0)	2.92 (19.1)
K_2 based on transformed unsheared K's with V_f correction ($*10^{-10}$ m^2)	5.45	3.74 (10.2)	1.59 (56.0)
K_{2calc} with VGM (max nesting) ($*10^{-10}$ m^2)	4.01 (26.4)	3.96 (17.9)	4.05 (12.2)
K_{2calc} with VGM (layer/flat surface) ($*10^{-10}$ m^2)	12.6 (131)	12.6 (275)	12.1 (235)
K_{2calc} with VGM (4 layers in mold, no nesting) ($*10^{-10}$ m^2)	57.7 (959)	50.4 (1400)	48.3 (1240)

*Experimental values, values calculated with the transformation of unsheared permeabilities with and without volume fraction correction, and values calculated with variable gap model for all 3 cases investigated are shown. Percent errors with respect to corresponding experimental value are given in parentheses.

vious (acceptably aligned) layer. In the initial experiments performed for this work (Dungan et al., 1999) and in the further experiments performed in Parts I and II of the present portions of the work, these types of adjustments were routinely performed. We suspect that preferential nesting in the sheared versus the unsheared experiments may have played a role.

In contrast to one empirical model we compared to our data (Lai and Young, 1997), our numerical approach allows prediction of actual permeabilities, rather than ratios of principal permeabilities, in addition to flow front orientation. The difference is significant. Because of the large potential effect of nesting, we showed that reasonable bounds on actual permeability (using the 3D fabric model and the VGM) are relatively wide (i.e., greater than one order of magnitude) and of similar size to some discrepancies reported in the literature for fabrics tested under nominally similar conditions. Thus, one important conclusion of this work is that the transverse stacking is critically important in its effect on permeability. For manufacture of a relatively large part, however, entrapment of macroscopic voids is a key issue, in which case the orientation of the flow front through sections is

also critical. Our fundamental models predicted these with good accuracy.

This work suggests that the time-consuming bench-scale permeability database approach be supplanted by improved fabric models for low-pressure processes. Clearly, the effects of capillarity are small in such cases, as shown by the good agreement here even for intratow permeability neglected (and validated with more detailed simulations as well at the tow level).

An artifact of use of the present VGM, or variable gap model, is the irregularity in the calculated permeability curves. This is a result of the 1D nature of the calculation: instead of flow being allowed to meet transverse to the direction studied, flow proceeds in 1D. In a real setting, the melding of flow fronts moving radially outward would significantly smooth the flow pattern. Work here suggests that 2D flow models may actually be unnecessary, however, for simple cases, in favor of careful consideration of how to calculate critical angles.

NOMENCLATURE

a_i	thickness of equivalent channel at either end (i = 1,2)
A	distance between either ellipse focus and y axis
b	half of the distance between infinitely long plates
c	Kozeny constant
C_a	capillary number
d	diameter of a tube for circular Poiseuille flow
D	sum of distances between any point on ellipse and two foci
D_E	equivalent wetted diameter
F	shape factor for equivalent wetted diameter
F_i	external body force
g	gravitational acceleration
$2h$	thickness of a fabric layer
K	permeability
K_X	axial permeability
K_Z	transverse permeability
K_{it}	tow permeability
K_{rep}	representative permeability
L_{sect}	length of a complete or completed cross-section
N	number of points on ellipse
P	pressure
∇P	pressure gradient
P^c	capillary pressure
(P_i, Q_i)	ith data point
r_f	fiber radius
r_{fA}	micro-front radius
r_{1A}	tow radii

r_{2A} cell radii
S length of a fabric representative unit cell
t time
v_{ave} average flow front velocity
v velocity
$\bar{v}$ average fluid velocity
V_f volume fraction
V_A maximum packing capacity
w yarn width
x_{inter} reference point on the x-axis
(x_i, y_i) ith point on ellipse
X flow progression length
α_i critical angles (i = 1,2)
β half period of sinusoid describing yarn cross-section
γ_{maxi} maximum flow angles based on critical angles (i = 1,2)
γ_{mini} minimum flow angles based on critical angles (i = 1,2)
ε porosity
η principal flow angle
θ shear angle
90-θ angle between warp and weft
χ cross-section angle
μ viscosity
ρ density
ψ contact angle
σ surface tension
τ shear stress

Subscripts

0 value in the unsheared configuration
a value in the warp direction
b value in the weft direction
calc calculated value
exp experimental value
sat saturated value
unsat unsaturated value

Abbreviations

r.c. representative cell
err error
VGM variable-gap model

ACKNOWLEDGEMENTS

The authors gratefully acknowledge support for this project from the U.S. Army TACOM, General Motors, the NSF SIUCRC on Low Cost, High Speed Polymer Composite Processing, and a National Science Foundation PECASE grant. Support for FDD from a François-Xavier Bagnoud fellowship (Department of Aerospace Engineering, University of Michigan) is also gratefully acknowledged.

REFERENCES

Adams, K.L. and L. Rebenfeld. 1991. "Permeability Characteristics of Multilayer Fiber Reinforcements. Part I: Experimental Observations," Polymer Composites, Vol. 12, No. 3, pp. 179–185.

Adams, K.L. and L. Rebenfeld. 1991. "Permeability Characteristics of Multilayer Fiber Reinforcements. Part II: Theoretical Model," Polymer Composites, Vol. 12, No. 3, pp. 186–190.

Ahn, K.J., J.C. Seferis, and J.C. Berg. 1991. "Simultaneous Measurements of Permeability and Capillary Pressure of Thermosetting Matrices in Woven Fabric Reinforcements," Polymer Composites, Vol. 12, No. 3, pp. 146–152.

Ambrosi, D. and L. Preziosi. 1998. "Modeling Matrix Injection through Elastic Porous Preforms," Composites Part A, Vol. 29, Nos. 1–2, pp. 5–18.

Batchelor, G.K. 1967. An Introduction to Fluid Dynamics, Cambridge: Cambridge University Press.

Berdichevsky, A.L. and Z. Cai. 1993. "Preform Permeability Predictions by Self-Consistent Method and Finite Element Simulation," Polymer Composites, Vol. 14, No. 2, pp. 132–143.

Binétruy C., B. Hilaire, and J. Pabiot. 1998. "Tow Impregnation Model and Void Formation Mechanisms during RTM," Journal of Composite Materials, Vol. 32, No. 3, pp. 223–245.

Blake, F.C. 1922. "The Resistance of Packing to Fluid Flow," Transactions of the American Institute of Chemical Engineers, Vol. 14, pp. 415–421.

Bruschke, M.V. and S.G. Advani. 1990. "A Finite Element/Control Volume Approach to Mold Filling in Anisotropic Porous Media," Polymer Composites, Vol. 11, No. 6, pp. 398–405.

Bruschke, M.V. and S.G. Advani. 1993. "Flow of Generalized Newtonian Fluids across a Periodic Array of Cylinders," Journal of Rheology, Vol. 37, No. 3, pp. 479–498.

Cai, Z. and A.L. Berdichevsky. 1993. "An Improved Self-Consistent Method for Estimating the Permeability of a Fiber Assembly," Polymer Composites, Vol. 14, No. 4, pp. 314–323.

Carman, P.C. 1937. "Fluid Flow through Granular Beds," Transactions of the Institution of Chemical Engineers (London), Vol. 15, pp. 150–156.

Chan, A.W., D.E. Larive, and R.J. Morgan. 1993. "Anisotropic Permeability of Fiber Preforms: Constant Flow Rate Measurement," Journal of Composite Materials, Vol. 27, No. 10, pp. 996–1008.

Chang, C.-Y. and L.-W. Hourng. 1998. "Numerical Simulation for the Transverse Impregnation in Resin Transfer Molding," Journal of Reinforced Plastics and Composites, Vol. 17, No. 2, pp. 165–182.

Chang, C.-Y., L.-W. Hourng, and C.-J. Wu. 1998. "Numerical Study on the Capillary Effect of Resin Transfer Molding," Journal of Reinforced Plastics and Composites, Vol. 16, No. 6, pp. 566–586.

Coulter, J.P. and S.I. Guceri. 1988. "Resin Transfer Molding: Process Review, Modeling and Research Opportunities," Proceedings of Manufacturing International '88, Atlanta, GA, pp. 79–86.

Darcy, H. 1856. Les Fontaines Publiques de la Ville de Dijon, Paris: Dalmont.

Dungan, F.D. 2000. "Investigation of Microscale Flow Phenomena in Determining Permeabilities of Fabrics for Composites." Ph.D. Thesis. University of Michigan.

Dungan, F.D., M.T. Senoguz, A.M. Sastry, and D.A. Faillaci. 1999. "On the Use of Darcy Permeability in Sheared Fabrics," Journal of Reinforced Plastics and Composites, Vol. 18, No. 5, pp. 472–484.

Dungan, F.D., M.T. Senoguz, A.M. Sastry, and D.A. Faillaci. 2001. "Simulations and Experiments on Low-Pressure Permeation of Fabrics: Part I—3D Modeling of Unbalanced Fabrics," Journal of Composite Materials, Vol. 35, No. 14, pp. 1250–1284.

FLUENT. 1998. *FLUENT 5 User's Guide Volume 1.*Lebanon, NH: Fluent Inc.

Gauvin, R., F. Trochu, Y. Lemenn, and L. Diallo. 1996. "Permeability Measurement and Flow Simulation through Fiber Reinforcement," Polymer Composites, Vol. 17, No. 1, pp. 34–42.

Gebart, B.R. 1992. "Permeability of Unidirectional Reinforcements for RTM," Journal of Composite Materials, Vol. 26, No. 8, pp.1100–1133.

Hourng, L.-W. and C.-Y. Chang. 1998. "The Influence of Capillary Flow on Edge Effect in Resin Transfer Molding," Journal of Reinforced Plastics and Composites, Vol. 17, No. 1, pp. 2–25.

Ismail, Y.M. and G.S. Springer. 1997. "Interactive Simulation of Resin Transfer Molding," Journal of Composite Materials, Vol. 31, No. 10, pp. 954–980.

Kolodziej, J.A., R. Dziecielak, and Z. Konczak. 1998. "Permeability Tensor for Heterogeneous Porous Medium of Fibre Type," Transport in Porous Media, Vol. 32, pp. 1–19.

Kozeny, J. 1927. "Ueber Kapillare Leitung des Wassers im Boden," Sitzungsberichte, Akademie der Wissenschaften in Wien, Vol. 136, pp. 271–301.

Kundu, P.K. 1990. Fluid Mechanics, San Diego: Academic Press.

Lai, C.-L. and W.-B. Young. 1997. "Model Resin Permeation of Fiber Reinforcements after Shear Deformation," Polymer Composites, Vol. 18, No. 5, pp. 642–648.

Lekakou, C. and M.G. Bader. 1998. "Mathematical Modeling of Macro and Micro-Infiltration in Resin Transfer Molding (RTM)," Composites Part A, Vol. 29A, pp. 29–37.

Lin, M., H.T. Hahn, and H. Huh. 1998. "A Finite Element Simulation of Resin Transfer Molding Based on Partial Nodal Saturation and Implicit Time Integration," Composites Part A, Vol. 29, Nos. 5–6, pp. 541–550.

Martin, G.Q. and J.S. Son. 1986. "Fluid Mechanics of Mold Filling for Fiber Reinforced Plastics," Proceedings of the Second Conference on Advanced Composites, 18–20 November 1986, Dearborn, MI, pp. 149–157.

Mogavero, J. and S.G. Advani. 1997. "Experimental Investigation of Flow through Multi-Layered Preforms," Polymer Composites, Vol. 18, No. 5, pp. 649–655.

Parnas, R.S., K.M. Flynn, and M.E. Dal-Favero. 1997. "A Permeability Database for Composites Manufacturing," Polymer Composites, Vol. 18, No. 5, pp. 623–633.

Pillai, K.M. and S.G. Advani. 1998. "Numerical Simulation of Unsaturated Flow in Woven Fiber Preforms during the Resin Transfer Molding Process," Polymer Composites, Vol. 19, No. 1, pp. 71–80.

Rudd, C.D., A.C. Long, P. McGeehin, and P. Smith. 1996. "In-Plane Permeability Determination for Simulation of Liquid Composite Molding of Complex Shapes," Polymer Composites, Vol. 17, No. 1, pp. 52–59.

Sastry, A.M. 2000. "Impregnation and Consolidation Phenomena," Vol. 2, Ch. 18 in *Comprehensive Composite Materials,* A. Kelly and C. Zweben (eds), Elsevier.

Scheidegger, A.E. 1974. The Physics of Flow through Porous Media, Toronto: University of Toronto Press, p. 58.

Shih, C.H. and L.J. Lee. 1998. "Effect of Fiber Architecture on Permeability in Liquid Composite Molding," Polymer Composites, Vol. 19, No. 5, pp. 626–639.

Skartsis, L., B. Khomami, and J.L. Kardos. 1992. "Resin Flow through Fiber Beds, Part I: Review of Newtonian Flow through Fiber Beds," Polymer Engineering and Science, Vol. 32, No. 4, pp. 221–230.

Skartsis, L., B. Khomami, and J.L. Kardos. 1992. "Resin Flow through Fiber Beds, Part II: Numerical and Experimental Studies of Newtonian Flow through Ideal and Actual Fiber Beds," Polymer Engineering and Science, Vol. 32, No. 4, pp. 231–239.

Skartsis, L., B. Khomami, and J.L. Kardos. 1992. "The Effect of Capillary Pressure on the Impregnation of Fibrous Media," SAMPE Journal, Vol. 28, No. 5, pp. 19–24.

Smith, P., C.D. Rudd, and A.C. Long. 1997. "The Effect of Shear Deformation on the Processing and Mechanical Properties of Aligned Reinforcements," Composites Science and Technology, Vol. 57, pp. 327–344.

Song, B., A. Bismarck, R. Tahhan, and J. Springer. 1998. "A Generalized Drop Length-Height Method for Determination of Contact Angle in Drop-on-Fiber Systems," Journal of Colloid and Interface Science, Vol. 197, No. 1, pp. 68–77.

Song, Y., W. Chui, J. Glimm, B. Lindquist, and F. Tangerman. 1997. "Applications of Front Tracking to the Simulation of Resin Transfer Molding," Computers and Mathematics with Applications, Vol. 33, No. 9, pp. 47–60.

Van der Westhuizen, J. and J.P. Du Plessis. 1996. "An Attempt to Quantify Fibre Bed Permeability Utilizing the Phase Average Navier-Stokes Equation," Composites Part A, Vol. 27A, pp. 263–269.

Wagner, H.D. 1990. "Spreading of Liquid Droplets on Cylindrical Surfaces: Accurate Determination of Contact Angle," Journal of Applied Physics, Vol. 67, No. 3, pp. 1352–1355.

Wang, C.Y. 1996. "Stokes Flow through an Array of Rectangular Fibers," International Journal of Multiphase Flow, Vol. 22, No. 1, pp. 185–194.

Williams, J.G., C.E.M. Morris, and B.C. Ennis. 1974. "Liquid Flow through Aligned Fiber Beds," Polymer Engineering and Science, Vol. 14, No. 6, pp. 413–419.

Young, W.-B. 1996. "The Effect of Surface Tension on Tow Impregnation of Unidirectional Fibrous Preform in Resin Transfer Molding," Journal of Composite Materials, Vol. 30, No. 11, pp. 1191–1209.

Young, W.-B. and S.F. Wu. 1995. "Permeability Measurement of Bidirectional Woven Glass Fibers," Journal of Reinforced Plastics and Composites, Vol. 14, pp. 1108–1120.